Sea Ice Flooding Observations via Remote Sensing

Laidlaw Research Report
June – July 2026

Stefani Naydenova, BEng
Mechanical Engineering

Supervised by Dr. Rosemary Willatt and PHD Student Alicia Fallows

1 Abstract

This study investigates whether sea ice flooding can be detected via remote sensing. Flooding usually results from a thick snow layer over thinner ice, leading to negative freeboard and seawater seeping into the snowpack. This process is identified in situ during field expeditions; the project explores if it can be discovered through remote observations. Two case studies with in situ flooding were selected. Remote sensing data came from NASA Earthdata's *AMSR-E/AMSR2 Unified L3 Daily 12.5 km Brightness Temperatures, Sea Ice Concentration, Motion & Snow Depth Polar Grids V001*. The flooding dates and coordinates from each study were recorded, and daily files covering those periods were downloaded from the dataset. Case 1 included the date of instalment of the ice floes which served as a baseline study. The hypothesis is that flooding can be detected remotely from changes in brightness temperature (TB). TB for a snowpack is surface temperature multiplied by emissivity. Following a flooding event, TB is expected to rise and then decrease once the water layer refreezes. Other components like gradient ratio (GR), the difference between brightness temperatures at two distinct frequencies, were considered. GR for flooded/wet snow is expected to be near 0. Both TB and GR plots for each case were produced. The brightness temperature plots in the base case appear lighter than in cases 1 and 2, in line with the hypothesis that in a flooding event, TB increases, making the plots appear darker. Moreover, the GR plots for the two cases appear relatively close to 0, further supporting the hypothesis. These results are promising. A next step would be to consider atmospheric conditions and look at climate data to check for rain or snow. This study will hopefully inspire additional research into remote sensing and its effectiveness in studying remote regions of the planet.

2 Introduction

2.1 Remote Sensing

Remote sensing refers to the collection of information from a distance (NASA Earthdata 2026a). Earth can be observed through remote instruments on satellites, spacecraft, or aircraft that detect and store reflected or emitted energy (NASA Earthdata 2026a). There are four types of remote sensing resolution: spatial, spectral, temporal, and radiometric (NASA Earthdata 2026b).

Radiometric resolution refers to the number of bits that outline the recorded energy (NASA Earthdata 2026b). When the radiometric resolution is high, there are more values to store information, which enables good discrimination between very small differences in energy. For instance, radiometric resolution is important in differentiating between small differences in ocean color, which is necessary for water quality assessments (NASA Earthdata 2026b).

Spatial resolution deals with the size of pixels within an image and the area that is represented by the specific pixel (NASA Earthdata 2026b). For instance, if there is a spatial resolution of 1km, each pixel represents a 1 km x 1km area on Earth. When the resolution is finer, more detail can be observed (NASA Earthdata 2026b).

Spectral resolution considers instruments' ability to detect finer wavelengths, which have a larger number or narrower bands. Most instruments have 3-10 bands and are multispectral (NASA Earthdata 2026b). Hyperspectral instruments have hundreds, even thousands of bands (NASA Earthdata 2026b).

Temporal resolution refers to the time required for a space-based platform to complete an orbit and return to the starting observation area (NASA Earthdata 2026b). It is dependent on the orbit, the characteristics of the instrument, and the swath width. Polar orbiting platforms have temporal resolution which can change from 1 day to 16 days (NASA Earthdata 2026b).

2.2 Active remote sensing

Active instruments send out an energy pulse which is reflected from the target and observe changes in the return signal (NASA Earthdata 2026c). Most of the active sensors work in the microwave band of the electromagnetic spectrum; this provides the opportunity to penetrate the atmosphere under various kinds of conditions (NASA Earthdata 2026c).

The following are the 6 categories of active instruments: laser altimeter, lidar, radar, ranging instrument, scatterometer, and sounder (NASA Earthdata 2026c).

More specifically, lidar is a light detection and ranging instrument (NASA Earthdata 2026c). It uses a laser radar to send a light pulse and a receiver with detectors that measure the reflected or backscattered light. The time between the transmitted and backscattered pulses is recorded and is used alongside the speed of light to calculate the distance to the object (NASA Earthdata 2026c).

Radar is a radio detection and ranging instrument which emits emits microwave radiation in pulses from an antenna (NASA Earthdata 2026c). Once the energy goes to the target, part of it is reflected back towards the instrument and is timed and measured (NASA Earthdata 2026c).

Scatterometer is a high-frequency microwave radar which is used to quantify backscattered radiation (NASA Earthdata 2026c).

Lastly, sounder explores the vertical distribution of precipitation alongside temperature, humidity, and cloud composition (NASA Earthdata 2026c).

2.3 Passive remote sensing

Passive instruments detect energy which is either emitted or reflected from an object (NASA Earthdata 2026d). They comprise various types of radiometers and spectrometers and operate in the visible, infrared, thermal infrared, and microwave parts of the electromagnetic spectrum (NASA Earthdata 2026d). The sensors analyze the temperature of land and sea surface, cloud and aerosol properties, as well as various physical attributes (NASA Earthdata 2026d). However, passive sensors usually can't penetrate dense cloud cover, which is why they aren't suitable in areas or times where dense cloud cover is present (NASA Earthdata 2026d).

There are various types of passive instruments. Accelerometer, which measures acceleration, and imaging radiometer, whose scanning capability can produce a two-dimensional array of pixels. An image can then be created from that array (NASA Earthdata 2026d). The scanning can happen mechanically or electronically with the use of detectors (NASA Earthdata 2026d).

Radiometers find the radiation power emmitted by the target in specific band ranges such as visible, infrared, and microwave (Kogut 2026). Hyperspectral radiometers detect a large number of narrow spectral bands in the visible, near-infrared, and mid-infrared portions of the electromagnetic spectrum (NASA Earthdata 2026d). Spectrometers detect and measure the spectral content of incident electromagnetic radiation, and imaging spectrometers often utilize gratings or prisms to disperse the radiation (NASA Earthdata 2026d).

2.3.1 Applications of Passive Remote Sensing

There are several examples of passive instruments and sensors in remote sensing. One example is Landsat, the longest lasting satellite mission to observe Earth (Kogut 2026). It monitored the planet and recorded data which tracked changes over a 40-year period. Interpretations are now applied in geology, mapping, meteorology, and more (Kogut 2026).

2.3.2 Microwave Remote Sensing

Passive microwave sensing monitors the microwave emissions from the objects (Kogut 2026). Passive sensors such as radiometers and scanners record natural energy and their antennas detect microwaves without further shorter waves. The signal allows specialists to learn about the temperature and moisture of the target (Kogut 2026). The detected radiation can be emitted by the target, transmitted, or reflected from it (Kogut 2026).

2.4 Flooding and snow-ice

Snow ice is formed when sea water floods the basal layers of the snowpack on sea ice and freezes (Ackley et al. 2020). Snow ice is found to be around 40% of the core length in the Bellingshausen and Amundsen Seas (Ackley et al. 2020). When sea ice has the oxygen isotopic signature close to snow, it is assumed to be snow ice (Ackley et al. 2020). In winter, the formation of snow ice is continuous for the most part across the Antarctic sea-ice zone. High ocean heat flux melts ice from the bottom (Ackley et al. 2020). On the top, there is redistribution and precipitation of snow (Ackley et al. 2020). These two processes cause the interface between snow and ice to be reduced below sea level, which results in flooding. When a warming event raises the upper ice temperature, this pushes sea water into the bottom snow layer and floods it (Ackley et al. 2020). A cold event later on freezes the snow-sea-water mixture and adds a layer of snow ice by freezing (Ackley et al. 2020).

In the Southern ocean, there are thick snow covers and thin ice, which is why insulation effect is more prevalent in comparison to the albedo effect (Wever et al. 2021a). Flooding and snow ice result from the thick snow on the thin ice. Sea water enters the snow caver through cracks in the ice or brine channels, and the flooding creates a layer at the bottom of the snow cover, which freezes to form snow ice (Wever et al. 2021a).

The snow cover on sea ice has effects on both thermal and mass balance of sea ice (Wever et al. 2021a). The high albedo of snow minimizes the absorption of shortwave radiation, which lowers the energy in the thermal balance (Wever et al. 2021a). Additionally, snow provides thermal insulation which reduces energy loss experienced by the sea ice. So snow impacts the sea ice thermal balance through albedo; melting snow has low albedo, while fresh snow has high albedo (Wever et al. 2021a).

Remote sensing has illustrated that snow cover and thickness of sea ice varies in the Southern Ocean within ocean basins (Wever et al. 2021a). Sea ice is thicker than 1 m in the western Weddell Sea, but it is thinner than 1 m in the eastern part. Moreover, snow depth is also different across the Southern Ocean and its maximum depth is in the western Weddell Sea and along the coast (Wever et al. 2021a). The spatial variability is in part due to ice age but also due to the roughness of sea ice since this provides spots where snow transported by wind can be collected (Wever et al. 2021a). Ice mass-balance buoys (IMBs) and snow buoys are utilized to measure the thickness of snow and ice. The devices are usually point measurements (Wever et al. 2021a).

Remote sensing methods usually capture large-scale spatial differences which go beyond meter-scale variability (Wever et al. 2021a). Airborne observations can capture the meter-scale fluctuations, but they have lower spatial and temporal scope (Wever et al. 2021a).

2.5 Case Review

2.5.1 Case 1

In a study conducted by Wever et al. in the Journal of Glaciology, IMBs were installed to measure sea ice temperatures continuously (Wever et al. 2021a). Each IMB was made up of a temperature sensor string (length 5 m) which has sensors placed every 2 cm (Wever et al. 2021a). Once daily, the sensor chain was heated to utilize the temperature response along the string and determine if the media around was ocean, sea ice or snow. The temperature and heating rate measurements help find out the following interfaces: ocean-sea ice, sea ice-snow, and snow-air (Wever et al. 2021a).

For the ice-ocean interface, it was identified through exploring the temperature gradient throughout the ice and seeing where the temperature stopped changing (Wever et al. 2021a). The snow-air interface was discovered in a similar way, but diurnal variation in the temperature profile was also considered given that air temperatures change more quickly in comparison to snow temperatures (Wever et al. 2021a).

Flooding was identified through variations in the heating rate profile at the base of the snow layer (Wever et al. 2021a). Flooded snow layers have very low heating rate since the liquid water in those layers has high heat capacity.

The accuracy of the interface findings was 2-4 cm, and the IMB had GPS receivers to measure the drift of the ice floes (Wever et al. 2021a).

2.5.2 Case 2

Satellite radar altimetry has been utilized to collect sea ice thickness changes in the Arctic (Willatt et al. 2010). There, the highest amplitude (Ku-band) radar return is assumed to come from the snow/ice interface given that the snow is both dry and cold (Willatt et al. 2010). However, in Antarctica, there is a more complicated snow stratigraphy. This is due, among other things, to higher temperatures in winter and snow flooding (Willatt et al. 2010). The paper by Willatt et al. presents the primary measurements of radar penetration into the snow cover of Antarctic sea ice (Willatt et al. 2010). The measurements cover the Ku-band, given that satellite radar altimeters operate at this frequency to measure snow depth. Data was collected in East Antarctica in September and October 2007 (Willatt et al. 2010). Radar data and field measurements of snow density, thickness, wetness, and the different layers was collected in several locations. Those included snow packs with flooding, hard crusts, and icy layers (Willatt et al. 2010).

Flooding was discovered at the first snowpit at Station 10, and the coordinates of the general area of Station 10 have been used for this study, taken from SIPEX data provided by Rosemary Willatt and Alicia Fallows: -65.94167, 119.13605.

3 Methods

The dataset used for this project is *AMSR-E/AMSR2 Unified L3 Daily 12.5 km Brightness Temperatures, Sea Ice Concentration, Motion & Snow Depth Polar Grids V001* and is from NASA Earthdata (Meier et al. 2018).

It shows 12.5 km spatial resolution and daily brightness temperatures which are horizontally and vertically polarized at 4 frequencies (Meier et al. 2018). The frequencies are 18.7 GHz, 23.8 GHz, 36.5 GHz and 89.0 GHz for ascending and descending orbits ((Meier et al. 2018)). The dataset also explores the daily sea ice concentrations which are estimated with the Enhanced NASA Team (NT2) algorithmn and daily snow depths over sea ice (Meier et al. 2018).

The study focuses on selecting the coordinates of ice floes where flooding has been observed in situ and assessing if these flooding events can be detected via remote sensing.

Two case studies were explored: case study 1 by Wever et al. (Wever et al. 2021a) and case study 2 by Willatt et al (Willatt et al. 2010). Python was used for data analysis and graph visualizations.

In case study 1, the IMB which was installed at station PS81/506 presented with flooding greater than 5 cm above the snow-ice interface (Wever et al. 2021a). This happened from 19 October 2013 onwards (Wever et al. 2021a). The station was installed on July 11 (start date) and was tracked for 4 initial days when the field team was doing transects (Wever et al. 2021a). The coordinates for PS81/506 are -67.356, -23.268 (Wever et al. 2021a). A base study was done with coordinates closest to this from the AMSR data, which were -65.675850, -23.268936. The timseries was July 11- July 14 2013, when no flooding was recorded. Daily data files corresponding to the dates of interest were downloaded from the dataset and used to generate plots for analysis.

However, it is important to note that after these days, the ice floe drifted further, which means that the flooding was observed in a different lat/lon. As a result, data was downloaded from supplementary files to the study as the IMBs had built in GPS. The following coordinates were selected from a table of lat/lons covering the dates of flooding: -66.0554, -20.303 (coordinates on October 25) and -66.4505, -18.338 (coordinates on November 5) (Wever et al. 2021b). The coordinates closest to those from Nasa Earthdata's dataset were -66.868195, -20.308441 and -66.319489, -18.347874. Daily files from the dataset were again downloaded - from end of October and beginning of November 2013.

In case study 2, as specific coordinates of the snow pit were not available, ones closest to the coordinates of Station 10 as previously presented were used for the investigation to see if flooding could be identified. From the AMSR data these were: -65.592354, 119.132378 and daily files were downloaded from end of September and beginning of October 2007.

3.1 Hypothesis

Passive microwave sensors detect the microwave energy that a snowpack emits (Liu et al. 2006). Brightness temperatures are calibrated from documented microwave energy and calculated through the following equation:

$$T_b = \varepsilon T_s \tag{1}$$

where Ts is the near-surface physical temperature of the snowpack and ε is its emissivity (Liu et al. 2006).

The increase in the liquid water content makes the wet snow act as a black body and emit more energy (Liu et al. 2006). Therefore, the hypothesis is that following a flooding event, brightness temperature is expected to rise. Once the water layer refreezes, brightness temperature is expected to decrease because the reestablished ice particles scatter radiation emitted from deeper snow (Liu et al. 2006).

With flooding, seawater or brine can infiltrate the snow (via mechanisms presented in Section 2.4), which leads to slush and usually subsequent snow ice (Zhou et al. 2024). This makes up about one third of the total sea ice mass in Antarctica (Zhou et al. 2024). Various processes happen at the snow ice interface like further seeping of seawater into the snowpack and drainage of brine within the snow ice that has been formed (Zhou et al. 2024). The brine in sea ice can come up into the basal snow layer via capillary suction, which leads to brine-wetted snow but may or may not be classified as flooding depending on the amount of liquid water. Besides this, in winter, atmospheric forcings, precipitation changes, strong winds, and multiple melt-refreeze cycles all lead to a complex snow stratigraphy (Zhou et al. 2024). This results in changes in snow grain size and density and refreezing under or within the snow cover, which impact the snow's thermodynamic properties and surface albedo (Zhou et al. 2024). There are also changes in the snow's dielectric properties, which affects microwave emissivity and the collection of different sea ice parameters (Zhou et al. 2024).

Microwave emission from the sea ice covered in snow is determined by grain size, density, liquid water content, and salinity, but the characteristics of each layer also have an impact (Zhou et al. 2024). Wet and saline snow are absorbent of microwave emissions (Zhou et al. 2024). Even when the snow is dry, differences in grain size and density can impact microwave emission. The main obstacle is to determine how these physical snow attributes impact microwave emissions (Zhou et al. 2024), and in this study if basal flooding can be identified in isolation from the microwave emission data.

3.2 Further Equations

3.2.1 Gradient Ratio

The formula compares the brightness temperature at two distinct microwave frequencies (Surdyk & Fily 1993):

$$GR_i(f_2 - f_1) = \frac{TB_i(f_2) - TB_i(f_1)}{TB_i(f_2) + TB_i(f_1)} \tag{2}$$

i stands for polarization, which can be either horizontal or vertical (Surdyk & Fily 1993).

Within a snowpack, volume scattering of microwaves gets larger with frequency and reduces sea ice brightness temperature quicker at higher frequencies with increasing snow thickness (Nelson et al. 2026). This is quantified by the gradient ratio, which is the normalized difference in brightness temperature at two distinct frequencies (Nelson et al. 2026). GR is commonly used in snow depth retrieval studies (Nelson et al. 2026).

In the microwave region, volume scattering within the snow has an effect on the radiation which is emitted from the ice underneath and, as a result, changes the brightness temperature (Rostosky et al. 2018). A negative gradient ratio could be observed with thicker snow cover because as snow deepens, there is more radiation scattering and the brightness temperature at the snow surface decreases with increasing frequency (Rostosky et al. 2018). For this project, the hypothesis is that the gradient ratio for flooded/wet snow is near 0 given that in wet snow conditions, the liquid water in the snowpack absorbs microwave energy which decreases backscatter (Hoppinen et al. 2024).

However, it is important to note that there are some limitations with satellite-derived snow depth products for Antarctic sea ice. Firstly, the algorithms assume dry snow even though a large portion of Antarctic snow is not dry and there is no information of where the snow is wet nor how wet it is (C. Nelson, personal communication, 16 July 2026). Secondly, Antarctic snow depth is deep and the algorithms typically use frequencies that saturate at 0.5 m, which means there is no way to analyze past this point (C. Nelson, personal communication, 16 July 2026).

3.2.2 Haversine Formula

Haversine formula finds the distance between 2 points based on the length of the straight line between them on the longitude and latitude (Azdy & Darnis 2020). In order to calculate the distance, the difference in latitude Δlat and longitude Δlon in radians of the two coordinate points is required (Azdy & Darnis 2020).

$$\Delta\text{lat} = \text{latitude}_2 - \text{latitude}_1 \tag{3}$$

$$\Delta\text{lon} = \text{longitude}_2 - \text{longitude}_1 \tag{4}$$

The distance is then calculated as follows, using Earth's radius R = 6371 km (Azdy & Darnis 2020):

$$\text{distance} = 2 \cdot R \cdot \arcsin\left(\sqrt{\sin^2\left(\frac{\Delta\text{lat}}{2}\right) + \cos(\text{latitude}_2) \cdot \cos(\text{latitude}_1) \cdot \sin^2\left(\frac{\Delta\text{lon}}{2}\right)}\right) \tag{5}$$

In the study, the formula is used to calculate the heights and widths of both the gradient ratio and brightness temperature zoomed out plots (which are displayed in the Results section).

4 Results

4.1 Case 1 in the Weddell Sea Area

4.1.1 Base Case - Initial Installation of the Ice Station PS81/506 from the Study Conducted by Wever et al.

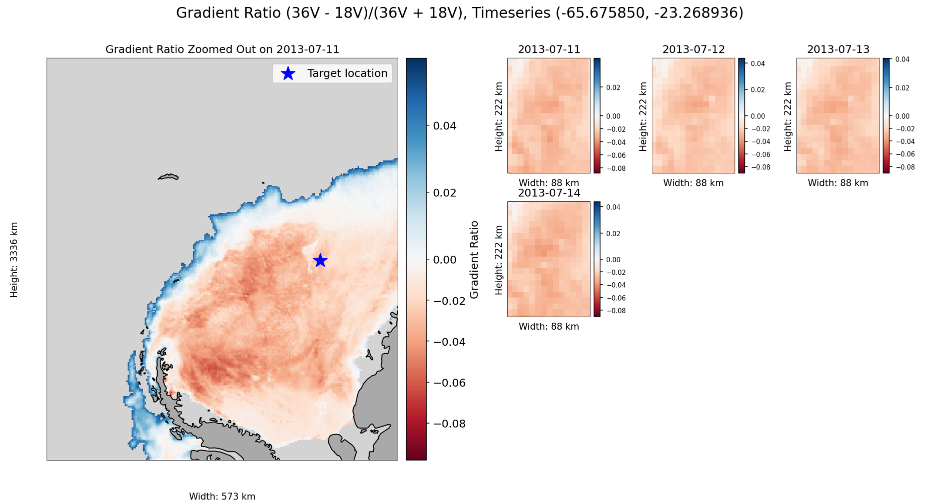

Figure 1: Gradient Ratio (18.7 GHz and 36.5 GHz), DAY, Vertical Polarization, July 11 - July 14, 2013. Zoomed in graphs on the right are 1 degree radius around the target location of -65.67585 °, -23.268936 °which is closest to -67.356 °, -23.268 °(ice station PS81/506)

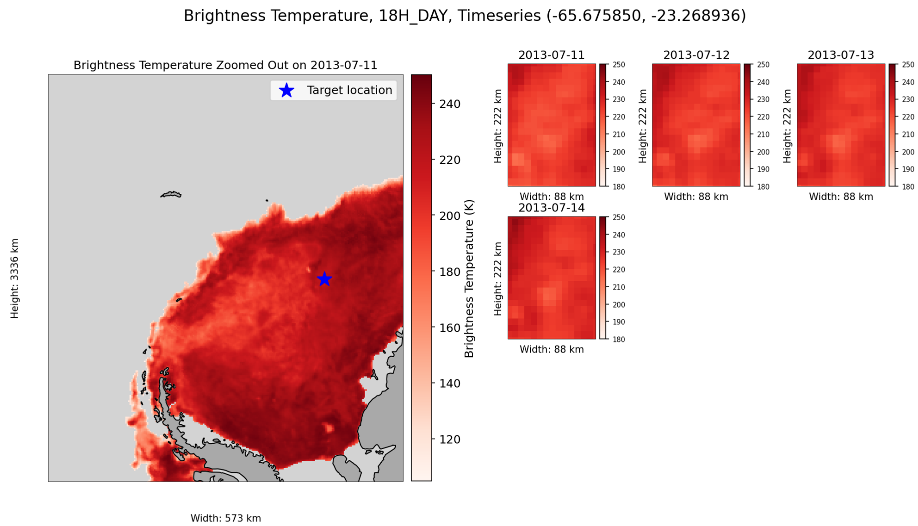

Figure 2: Brightness Temperature at 18.7 GHz, DAY, Horizontal Polarization, July 11 - July 14, 2013. Zoomed in graphs on the right are 1 degree radius around the target location of -65.67585 °, -23.268936 °

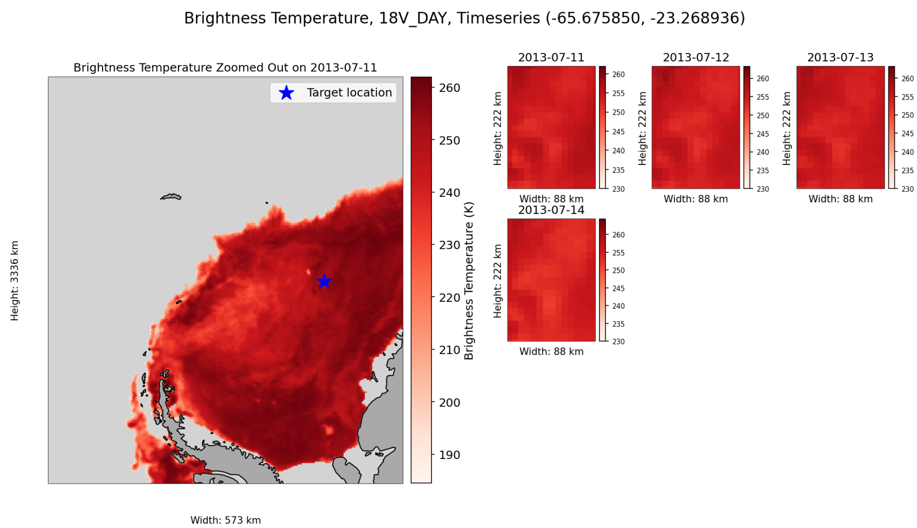

Figure 3: Brightness Temperature at 18.7 GHz, DAY, Vertical Polarization, July 11 - July 14, 2013. Zoomed in graphs on the right are 1 degree radius around the target location of -65.67585 °, -23.268936 °

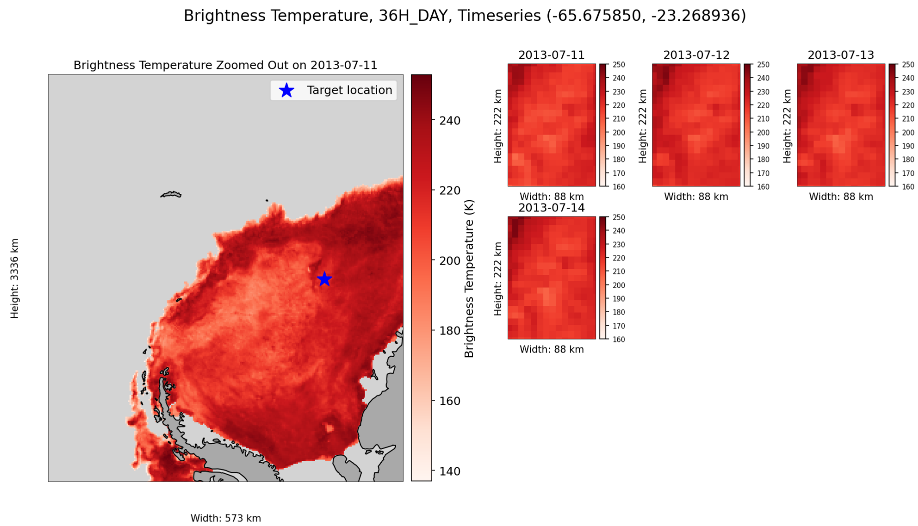

Figure 4: Brightness Temperature at 36.5 GHz, DAY, Horizontal Polarization, July 11 - July 14, 2013. Zoomed in graphs on the right are 1 degree radius around the target location of -65.67585 °, -23.268936 °

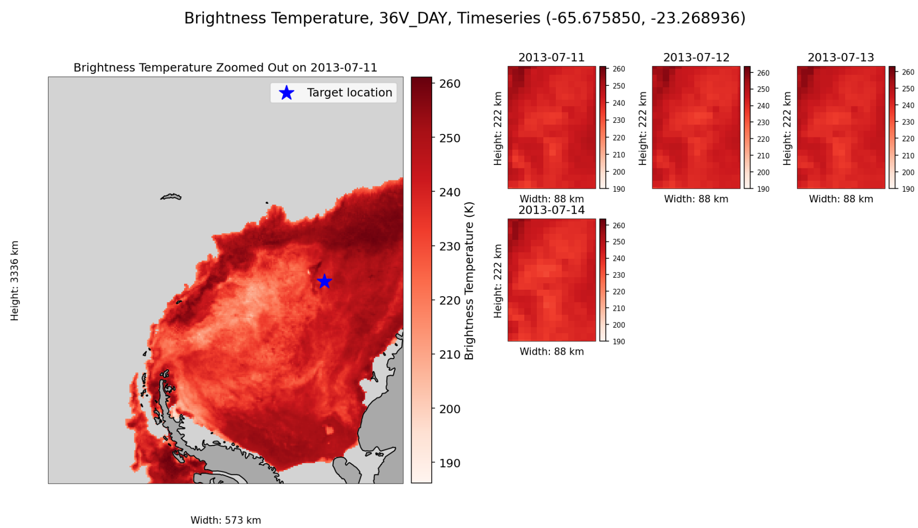

Figure 5: Brightness Temperature at 36.5 GHz, DAY, Vertical Polarization, July 11 - July 14, 2013. Zoomed in graphs on the right are 1 degree radius around the target location of -65.67585 °, -23.268936 °

4.1.2 Flooding Coordinates 1.0 Accounting for Ice Floe Drift (End of October - Early November)

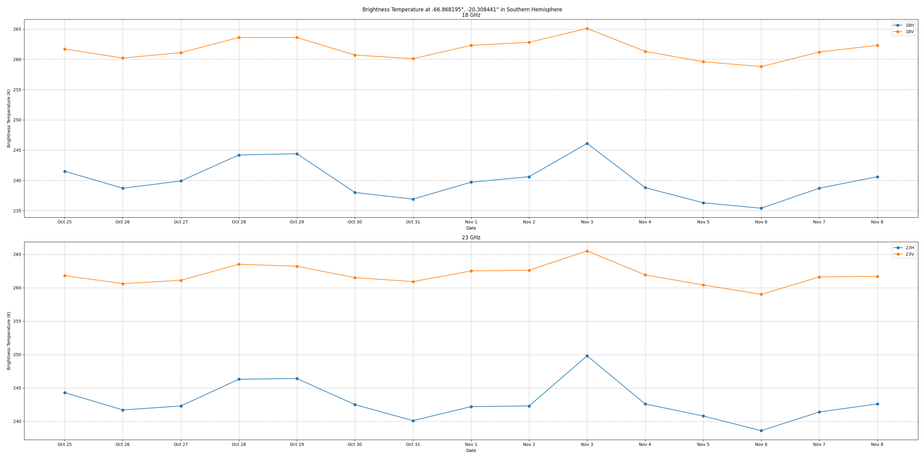

Figure 6: Brightness Temperature for a Single Pixel at -66.868195 °, -20.308441 °, which is closest to -66.0554 °, -20.303 °, October 25 - Nov 8, 2013 at 18.7 GHz and 23.8 GHz. These are the coordinates of the ice floe on October 25, 2013

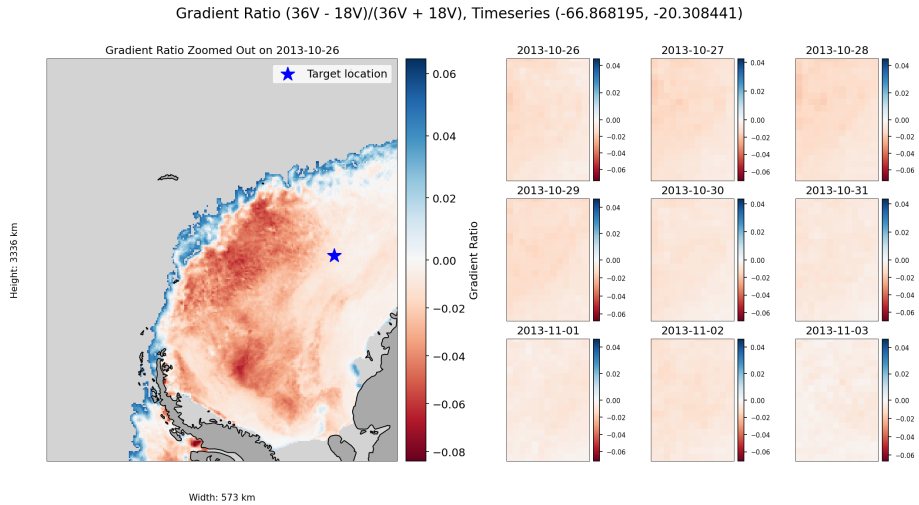

Figure 7: Gradient Ratio (18.7 GHz and 36.5 GHz), DAY, Vertical Polarization, October 25 - November 3, 2013. Zoomed in graphs on the right are 1 degree radius around the target location of -66.868195 °, -20.308441 °

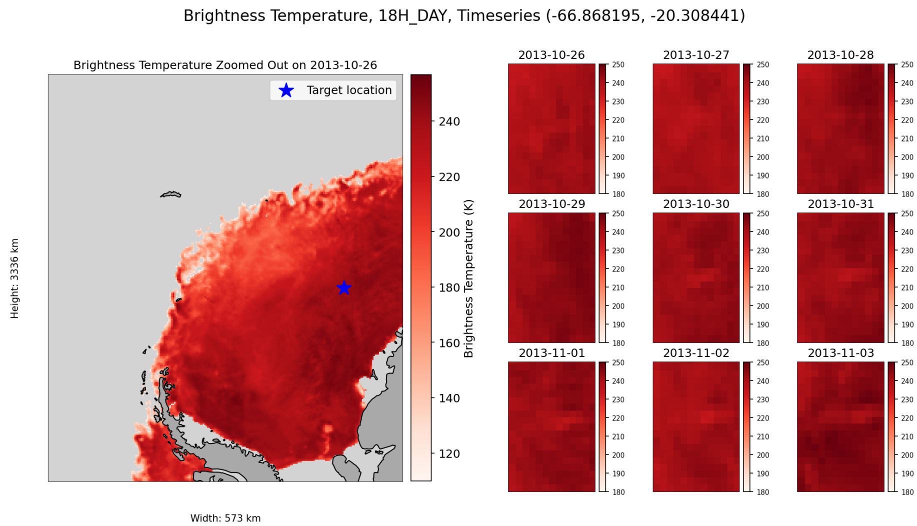

Figure 8: Brightness Temperature at 18.7 GHz, DAY, Horizontal Polarization, October 25 - November 3, 2013. Zoomed in graphs on the right are 1 degree radius around the target location of -66.868195 °, -20.308441 °

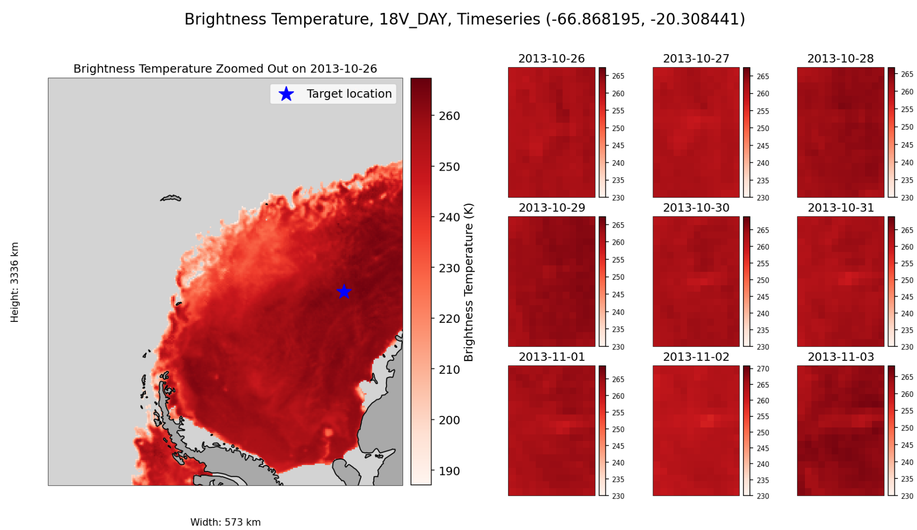

Figure 9: Brightness Temperature at 18.7 GHz, DAY, Vertical Polarization, October 25 - November 3, 2013. Zoomed in graphs on the right are 1 degree radius around the target location of -66.868195 °, -20.308441 °

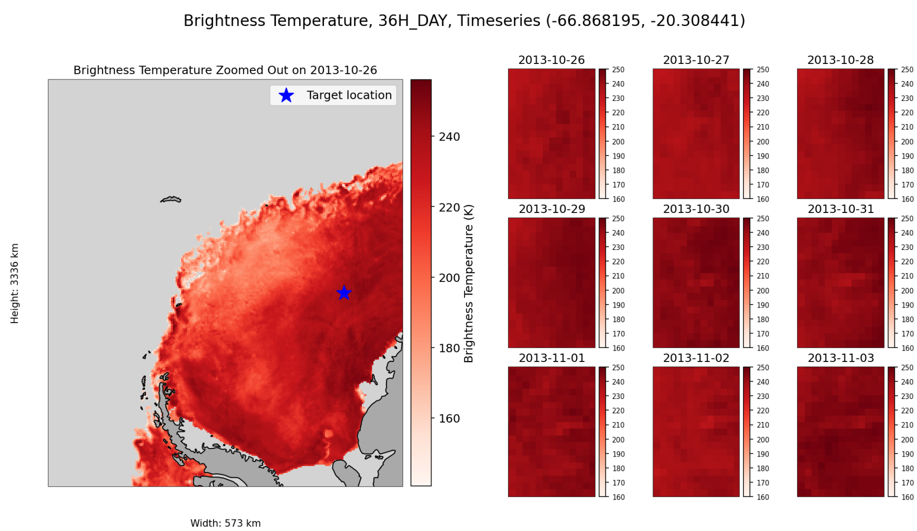

Figure 10: Brightness Temperature at 36.5 GHz, DAY, Horizontal Polarization, October 25 - November 3, 2013. Zoomed in graphs on the right are 1 degree radius around the target location of -66.868195 °, -20.308441 °

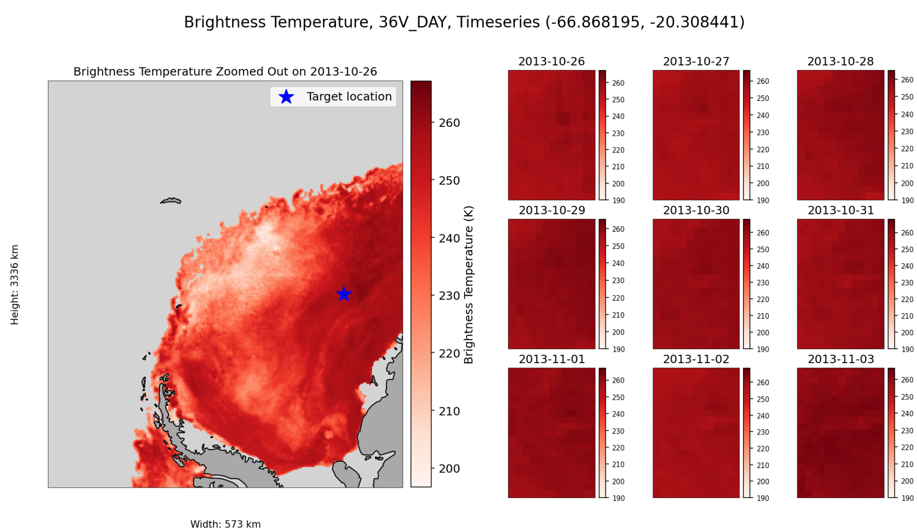

Figure 11: Brightness Temperature at 36.5 GHz, DAY, Vertical Polarization, October 25 - November 3, 2013. Zoomed in graphs on the right are 1 degree radius around the target location of -66.868195 °, -20.308441 °

4.1.3 Flooding Coordinates 2.0 Accounting for Ice Floe Drift (End of October - Early November)

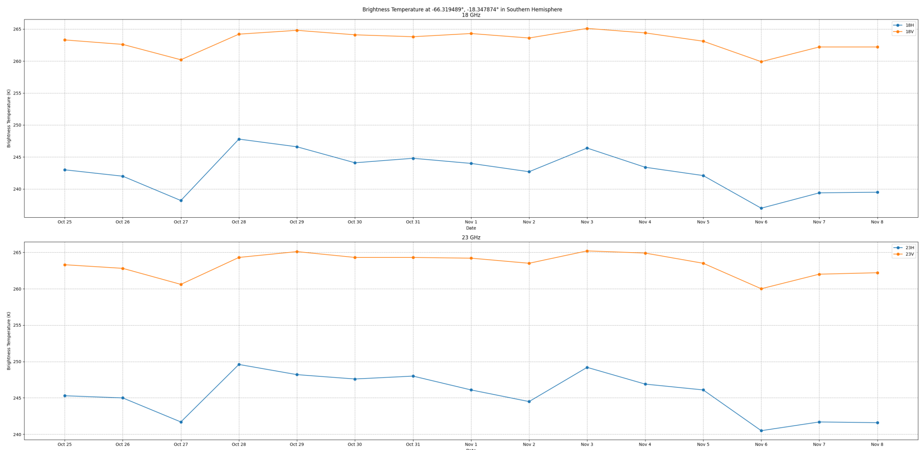

Figure 12: Brightness Temperature for a Single Pixel at -66.319489 °, -18.347874 °, which is closest to -66.4505 °, -18.338 °, October 25 - Nov 8, 2013 at 18.7 GHz and 23.8 GHz. These are the coordinates of the ice floe on November 5, 2013

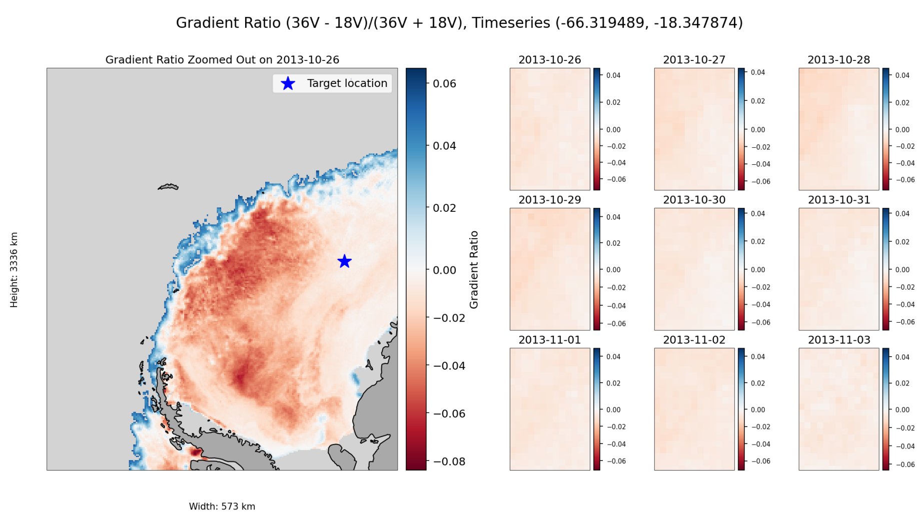

Figure 13: Gradient Ratio (18.7 GHz and 36.5 GHz), DAY, Vertical Polarization, October 25 - November 3, 2013. Zoomed in graphs on the right are 1 degree radius around the target location of -66.319489 °, -18.347874 °

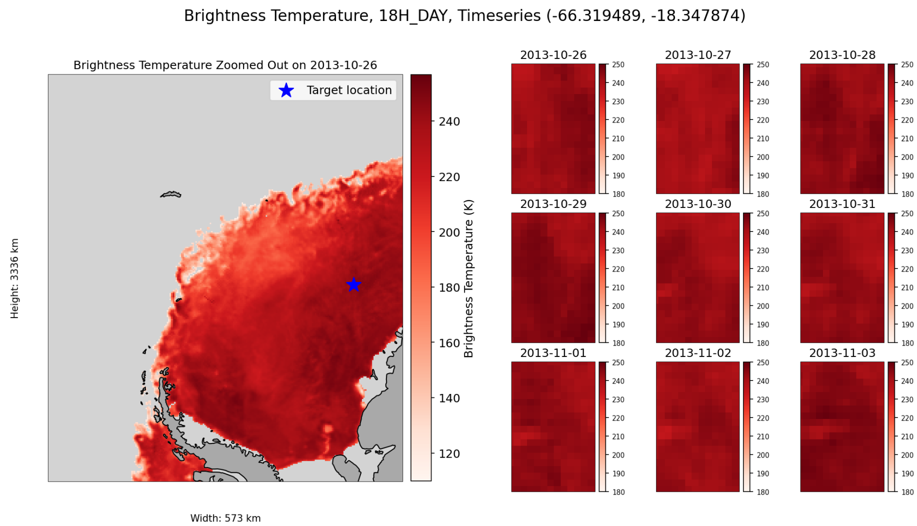

Figure 14: Brightness Temperature at 18.7 GHz, DAY, Horizontal Polarization, October 25 - November 3, 2013. Zoomed in graphs on the right are 1 degree radius around the target location of -66.319489 °, -18.347874 °

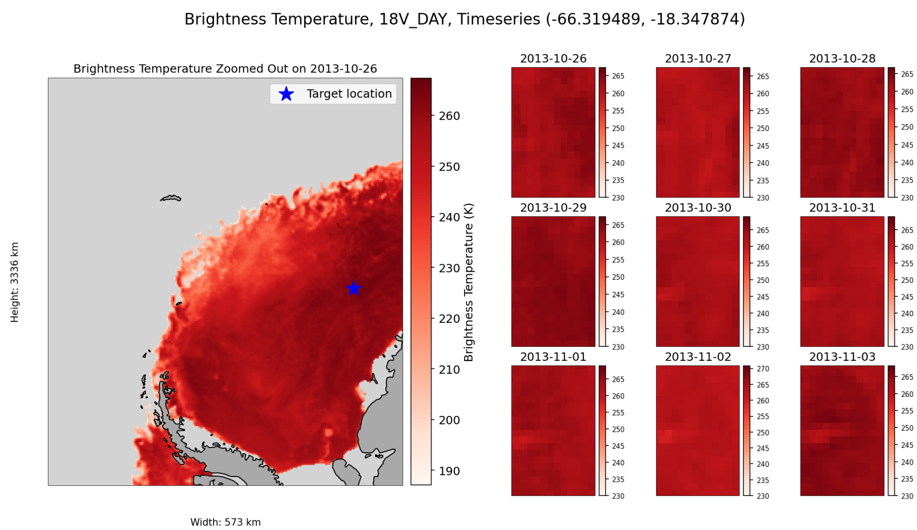

Figure 15: Brightness Temperature at 18.7 GHz, DAY, Vertical Polarization, October 25 - November 3, 2013. Zoomed in graphs on the right are 1 degree radius around the target location of -66.319489 °, -18.347874 °

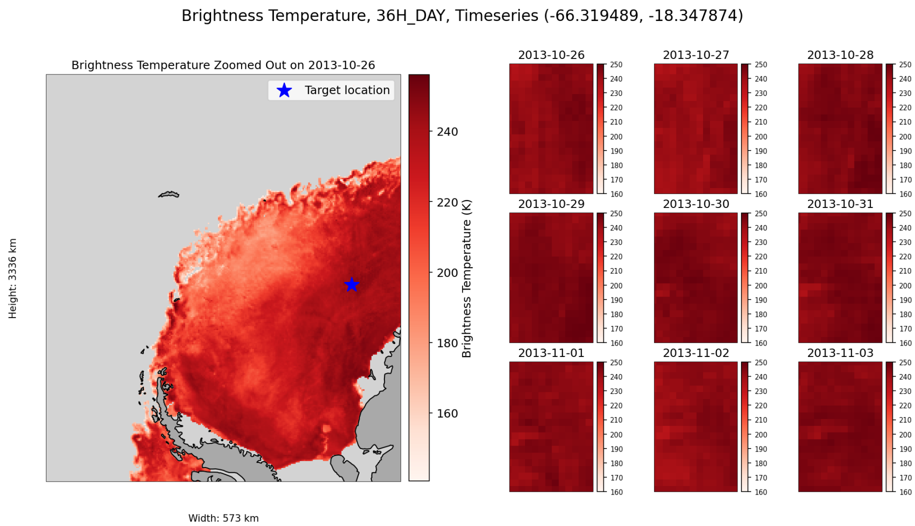

Figure 16: Brightness Temperature at 36.5 GHz, DAY, Horizontal Polarization, October 25 - November 3, 2013. Zoomed in graphs on the right are 1 degree radius around the target location of -66.319489 °, -18.347874 °

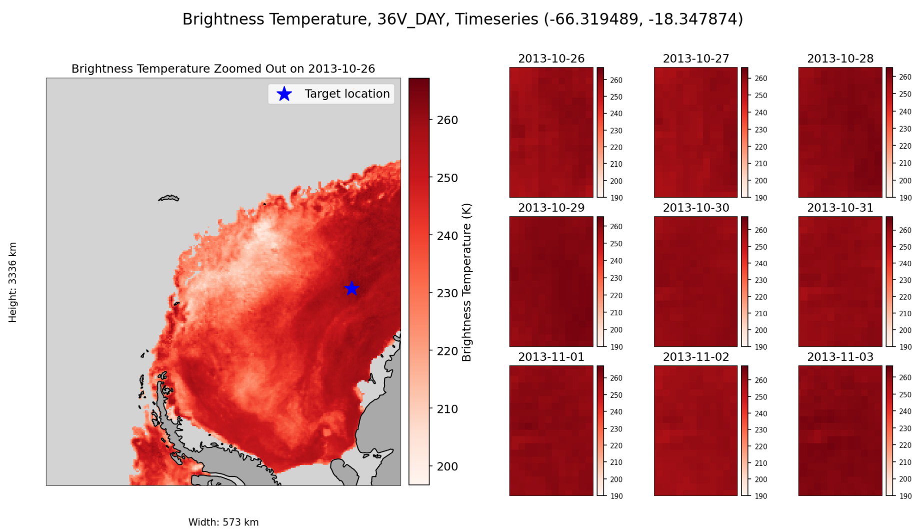

Figure 17: Brightness Temperature at 36.5 GHz, DAY, Vertical Polarization, October 25 - November 3, 2013. Zoomed in graphs on the right are 1 degree radius around the target location of -66.319489 °, -18.347874 °

4.2 Case 2 in the Western Pacific (off the Coast of East Antarctica

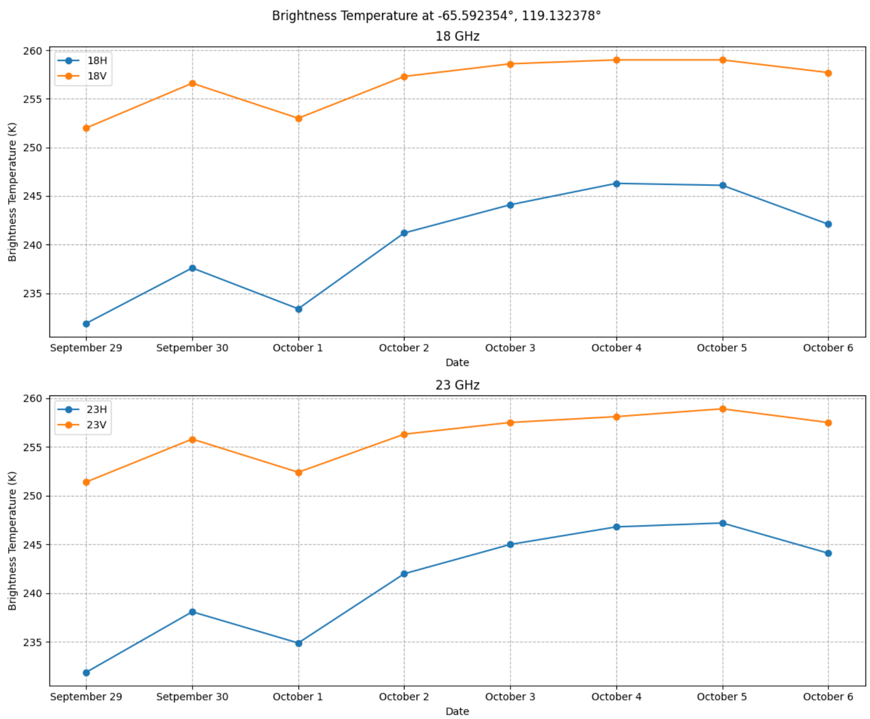

Figure 18: Brightness Temperature for a Single Pixel at -65.592354 °, 119.132378 °, September 29 - October 6, 2007 at 18.7 GHz and 23.8 GHz

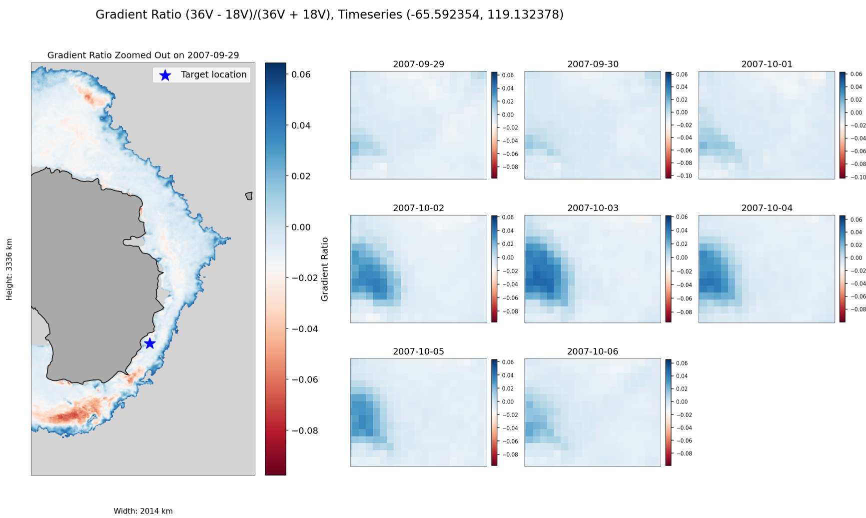

Figure 19: Gradient Ratio (18.7 GHz and 36.5 GHz), DAY, Vertical Polarization, September 29 - October 6, 2007. Zoomed in graphs on the right are 1 degree radius around the target location of -65.592354 °, 119.132378 °

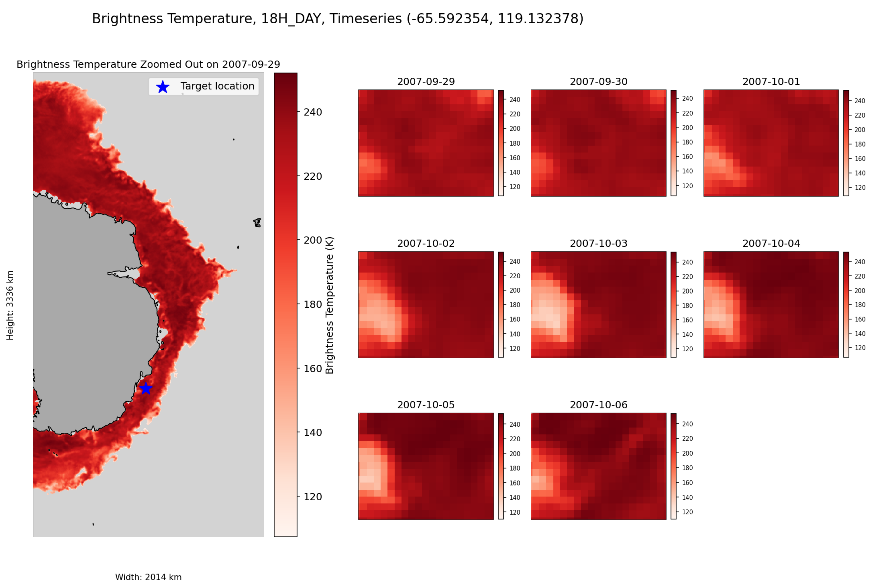

Figure 20: Brightness Temperature at 18.7 GHz, DAY, Horizontal Polarization, September 29 - October 6, 2007. Zoomed in graphs on the right are 1 degree radius around the target location of -65.592354 °, 119.132378 °

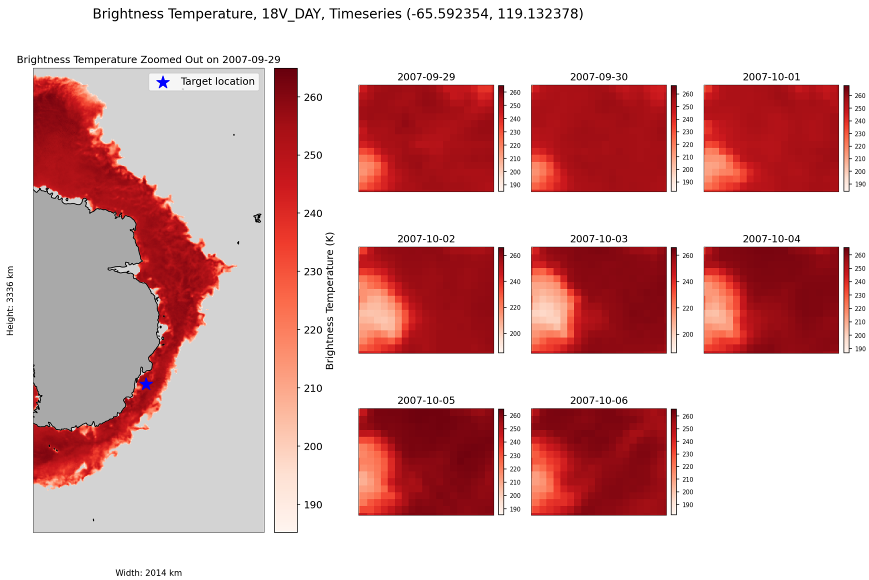

Figure 21: Brightness Temperature at 18.7 GHz, DAY, Vertical Polarization, September 29 - October 6, 2007. Zoomed in graphs on the right are 1 degree radius around the target location of -65.592354 °, 119.132378 °

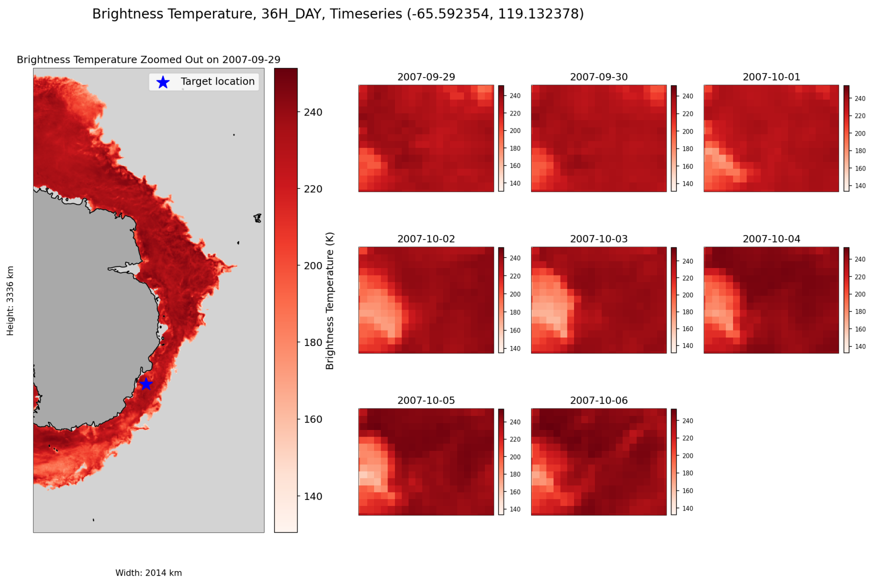

Figure 22: Brightness Temperature at 36.5 GHz, DAY, Horizontal Polarization, September 29 - October 6, 2007. Zoomed in graphs on the right are 1 degree radius around the target location of -65.592354 °, 119.132378 °

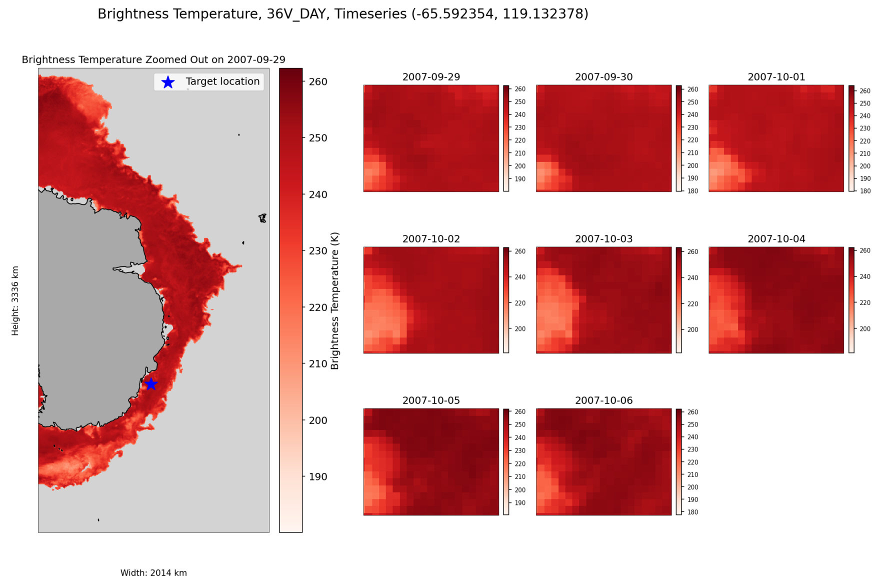

Figure 23: Brightness Temperature at 36.5 GHz, DAY, Vertical Polarization, September 29 - October 6, 2007. Zoomed in graphs on the right are 1 degree radius around the target location of -65.592354 °, 119.132378 °

5 Discussion

Antarctica has been losing its ice mass since 2002 at an average rate of 130 billion metric tons per year (NASA Science no date). There has also been increased snowfall (European Space Agency 2026). A factor which has led to increased snowfall volume is the movement of moisture in the atmosphere through atmospheric rivers that carry large amounts of water vapour (European Space Agency 2026). Researchers who have studied the atmospheric rivers that reach Antarctica have found that rivers were more common and fierce as of 2020 (European Space Agency 2026). Strong westerly winds helped to transport more water vapour over the continent (European Space Agency 2026). This relates to how flooding usually occurs when there is a thick snow cover over a thin ice layer.

In this project, the base case for flooding is taken to be the period when an ice floe station was installed in July 2013. The brightness temperature cartopy plots from this period are considerably lighter than those from October and November 2013, when flooding was observed in situ in case study 1. The base case plots are also lighter than those from September 2007 in case study 2. These results are consistent with the hypothesis that flooding leads to an increase in brightness temperature, which would make the plots appear darker.

Regarding the base case gradient ratio plots from July 2013, they are predominantly red, with values approaching the negative end of the colorbar, which is consistent with a thicker snow cover. In case 1, the GR plots from October and November 2013 become lighter and move toward zero. In case 2, the plots are blue, with small positive values that also lie close to zero. In both cases, this could suggest that the snow during these periods is wet or flooded, in line with the comments on equation 2.

However, it is important to note that atmospheric condition heavily interfere and this project didn't include meteorology data. An important next step would be to look at climate data and see whether in the periods of interest it rained or snowed. This would help inform the conclusion of whether or not the brightness temperature changes can be attributed solely to flooding and if flooding can be identified via remote sensing. Additionally, case study 1 could be extended back to prior to October 19th 2013, when flooding was first identified by the IMB, to see if there is a clear jump/change around this date. Overall, increasing the timeseries would help to understand what is a significant change in brightness temperature rather than frequent fluctuation, though care should still be taken to compare with climatic data.

6 Conclusion

This project aimed to explore sea ice flooding via remote sensing. The hypothesis was that flooding could be identified through changes in the brightness temperature. After a flooding event, an increase in brightness temperature is expected and then a decrease after refreezing.

Two case studies where flooding was found in situ were analyzed. The dates and coordinates of the flooded ice floes served as guidance on what data to download from the AMSR-E/AMSR2 dataset. The downloaded data was used to create plots to conduct analysis.

Overall, a rise in the brightness temperature was observed, which in line with the stated hypothesis, shows a flooding event could have occurred, but further analysis on atmospheric conditions is necessary.

7 Acknowledgements

Rosemary Willatt secured funding for this project via UCL's Laidlaw Leadership and Research Programme and proposed the concept, suggesting supervision support from her PhD student Alicia Fallows whose project is on flooding of snow on sea ice.

Detailed ideas for the project and case study approach / methodology were developed by Alicia Fallows, based on discussions with and ideas from Rosemary Willatt and Stefan Kern around the question 'How can we detect flooded/wet snow at scale from remote sensing?'. Stefan Kern encouraged using passive microwave data and studying areas of known flooding, providing a basis for the methodology.

The code for the cartopy plots was based on Connor Nelson's Github repository titled 'ROSPassiveImpact'.

This project is made possible via the Laidlaw foundation.

References

Ackley, S. F., Perovich, D. K., Maksym, T., Weissling, B. & Xie, H. (2020), 'Surface Flooding of Antarctic Summer Sea Ice', *Annals of Glaciology* **61**(82), 117–126. doi: 10.1017/aog.2020.22. (Accessed: 22 June 2026).

Azdy, R. A. & Darnis, F. (2020), 'Use of Haversine Formula in Finding Distance between Temporary Shelter and Waste End Processing Sites', *Journal of Physics: Conference Series* **1500**(1), 012104. doi: 10.1088/1742-6596/1500/1/012104. (Accessed: 13 July 2026).

European Space Agency (2026), 'Why is Antarctica's Mass Increasing?'. Available at: `https://www.esa.int/Applications/Observing_the_Earth/FutureEO/Space_for_our_climate/Why_is_Antarctica_s_mass_increasing` (Accessed: 10 August 2026).

Hoppinen, Z., Palomaki, R. T., Brencher, G., Dunmire, D., Gagliano, E., Marziliano, A., Tarricone, J. & Marshall, H.-P. (2024), 'Evaluating Snow Depth Retrievals from Sentinel-1 Volume Scattering over NASA SnowEx Sites', *The Cryosphere* **18**(11), 5407–5430. doi: 10.5194/tc-18-5407-2024. (Accessed: 29 June 2026).

Kogut, P. (2026), 'Types of Remote Sensing: Technology Changing the World', Available at: `https://eos.com/blog/types-of-remote-sensing/`. (Accessed: 19 June 2026).

Liu, H., Wang, L. & Jezek, K. C. (2006), 'Spatiotemporal Variations of Snowmelt in Antarctica Derived from Satellite Scanning Multichannel Microwave Radiometer and Special Sensor Microwave Imager Data (1978–2004)', *Journal of Geophysical Research: Earth Surface* **111**(F1). doi: 10.1029/2005JF000318. (Accessed: 22 June 2026).

Meier, W. N., Markus, T. & Comiso, J. C. (2018), 'AMSR-E/AMSR2 Unified L3 Daily 12.5 km Brightness Temperatures, Sea Ice Concentration, Motion & Snow Depth Polar Grids, Version 1', [Dataset]. NASA National Snow and Ice Data Center Distributed Active Archive Center. Available at: https://doi.org/10.5067/RA1MIJOYPK3P. (Accessed: 17 June 2026).

NASA Earthdata (2026a), 'Earth Observation Data Basics', Available at: `https://www.earthdata.nasa.gov/learn/earth-observation-data-basics`. (Accessed: 16 June 2026).

NASA Earthdata (2026b), 'Resolution', Available at: `https://www.earthdata.nasa.gov/learn/earth-observation-data-basics/remote-sensing-resolution`. (Accessed: 16 June 2026).

NASA Earthdata (2026c), 'Active Instruments', Available at: https://www.earthdata.nasa.gov/learn/earth-observation-data-basics/remote-sensing/active-instruments. (Accessed: 16 June 2026).

NASA Earthdata (2026d), 'Passive Instruments', Available at: https://www.earthdata.nasa.gov/learn/earth-observation-data-basics/remote-sensing/passive-instruments. (Accessed: 16 June 2026).

NASA Science (no date), 'Ice Sheets - Earth Indicator'. Available at: https://science.nasa.gov/earth/explore/earth-indicators/ice-sheets/ (Accessed: 10 August 2026).

Nelson, C., Stroeve, J., Lavergne, T., Landy, J., Willatt, R., Johnson, T., Baordo, F., Mallett, R. & Tsamados, M. (2026), 'Snow Depth on Arctic Sea Ice Retrieval Using a Synergy of Sentinel-3's Active and Passive Microwave Instruments', *Geophysical Research Letters* **53**(10). doi: 10.1029/2025GL121068. (Accessed: 29 June 2026).

Rostosky, P., Spreen, G., Farrell, S. L., Frost, T., Heygster, G. & Melsheimer, C. (2018), 'Snow Depth Retrieval on Arctic Sea Ice From Passive Microwave Radiometers-Improvements and Extensions to Multiyear Ice Using Lower Frequencies', *Journal of Geophysical Research* **123**(10), 7120–7138. doi: 10.1029/2018JC014028. (Accessed: 29 June 2026).

Surdyk, S. & Fily, M. (1993), 'Comparison of the Passive Microwave Spectral Signature of the Antarctic Ice Sheet with Ground Traverse Data', *Annals of Glaciology* **17**, 161–166. doi: 10.3189/S0260305500012775. (Accessed: 29 June 2026).

Wever, N., Leonard, K., Maksym, T., White, S., Proksch, M. & Lenaerts, J. T. M. (2021a), 'Spatially Distributed Simulations of the Effect of Snow on Mass Balance and Flooding of Antarctic Sea Ice', *Journal of Glaciology* **67**(266), 1055–1073. doi: 10.1017/jog.2021.54. (Accessed: 22 June 2026).

Wever, N., Maksym, T., White, S. & Leonard, K. C. (2021b), 'Ice Mass Balance Data PS81/506-1 from Weddell Sea, Antarctica, 2013-2014 [dataset]', *PANGAEA*. doi: 10.1594/PANGAEA.933417. (Accessed: 6 July 2026).

Willatt, R. C., Giles, K. A., Laxon, S. W., Stone-Drake, L. & Worby, A. P. (2010), 'Field Investigations of Ku-Band Radar Penetration Into Snow Cover on Antarctic Sea Ice', *IEEE Transactions on Geoscience and Remote Sensing* **48**(1), 365–372. doi: 10.1109/TGRS.2009.2028237. (Accessed: 29 June 2026).

Zhou, L., Stroeve, J., Nandan, V., Willatt, R., Xu, S., Zhu, W., Kacimi, S., Arndt, S. & Yang, Z. (2024), 'Quantifying the Influence of Snow Over Sea Ice Morphology on L-band Passive Microwave Satellite Observations in the Southern Ocean', *The Cryosphere* **18**(9), 4399–4434. doi: 10.5194/tc-18-4399-2024. (Accessed: 22 June 2026).